

Swelling and Evaporation Determine Surface Morphology of Grafted Hydrogel Thin Films

Caroline Kopecz-Muller, Clémence Gaunand, Yvette Tran, Matthieu Labousse, Elie Raphaël, Thomas Salez, Finn Box,* and Joshua D. McGraw*



Cite This: *Langmuir* 2025, 41, 2400–2410



Read Online

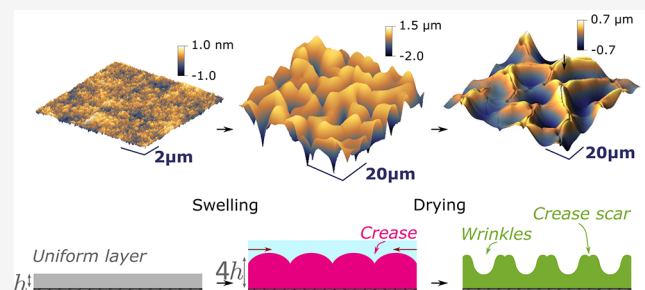
ACCESS |

Metrics & More

Article Recommendations

Supporting Information

ABSTRACT: We experimentally study the formation of surface patterns in grafted hydrogel films of nanometer-to-micrometer thickness during imbibition-driven swelling followed by evaporation-driven shrinking. Creases are known to form at the hydrogel surface during swelling; the wavelength of the creasing pattern is proportional to the initial thickness of the hydrogel film with a logarithmic correction that depends on microscopic properties of the hydrogel. We find that, although the characteristic wavelength of the pattern is determined during swelling, the surface morphology can be significantly influenced by evaporation-induced shrinking. We observe that the elastocapillary length based on swollen mechanical properties gives a threshold thickness for a surface pattern formation and consequently an important change in morphology.



INTRODUCTION

Smart hydrogels that respond to external stimuli enable the design of adaptive surface coatings.^{1,2} For example, grafted films of temperature-responsive hydrogels^{3–5} have been used in switchable microfluidic valves with rapid, reliable, and repeatable actuation^{6,7} and to trap single cells.⁸ These applications harness volume changes for functionality by exploiting the ability of polymers, in these cases poly(N-isopropylacrylamide) (PNIPAM), to swell in water, by about a factor 4, at room temperature.⁹ The resulting hydrogel exhibits a temperature-controlled transition between a swollen state, showing hydrophilic properties and elastic moduli in the kilopascal range, and a collapsed state, characterized by a hydrophobic behavior and a 100-fold stiffness increase.^{9–12} The switchable physicochemical properties of PNIPAM led to the design of media for controlled release in drug delivery systems.¹³ Furthermore, biocompatibility of PNIPAM is exploited by using films as substrates for cellular cultures and protein adsorption, as a bioscaffold in tissue engineering applications.¹⁴

Many of these applications require grafting the polymer to a substrate. Such grafting can constrain the swelling of hydrogel films and lead to surface patterning. Indeed, volumetric expansion associated with osmotic pressure is inhibited laterally by substrate-attachment. This geometrical frustration generates an in-plane compressive stress that can destabilize the flat surface of the hydrogel.^{15–19} This nonlinear instability^{20–22} renders the surface topography nonuniform, with sharp “creases” (localized regions of large strain/

curvature)²³ separating smooth peaks.^{15,24,25} Such creases are schematized in Figure 1A,B.

To date, the majority of the reported surface patterns occurred in wet hydrogel films of micrometric-to-millimetric thickness.^{3,15,26–30} Here, we report on a morphological transition on nanometric-to-millimetric gels that occurs upon drying, as illustrated in Figure 1A,B schematically, and in C and D from atomic force microscopy (AFM).

Surface patterns in soft cross-linked gels were first reported over a century ago³¹ and in swollen rubber in the 60s.³² A first theoretical prediction for surface instabilities occurring under in-plane compression was made by Biot.³³ In this prediction, on the condition that the in-plane strain exceeds a threshold of 0.46, an elastomeric half space deforms in a sinusoidal pattern, referred to as “wrinkles”.^{33,34} Later, Tanaka and coworkers investigated the formation and evolution of creases at the surface of synthetic gels during swelling.^{26,27} Unlike wrinkles that exhibit a sinusoidal shape, creases are characterized by localized regions of large, in-depth, surface curvature.

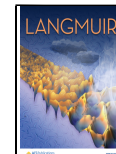
From the first observations of creases at the surface of gels and elastomers, further theoretical and numerical works,^{16,22,35} as well as experimental works^{15,21} showed that the creasing

Received: October 15, 2024

Revised: January 7, 2025

Accepted: January 8, 2025

Published: January 22, 2025



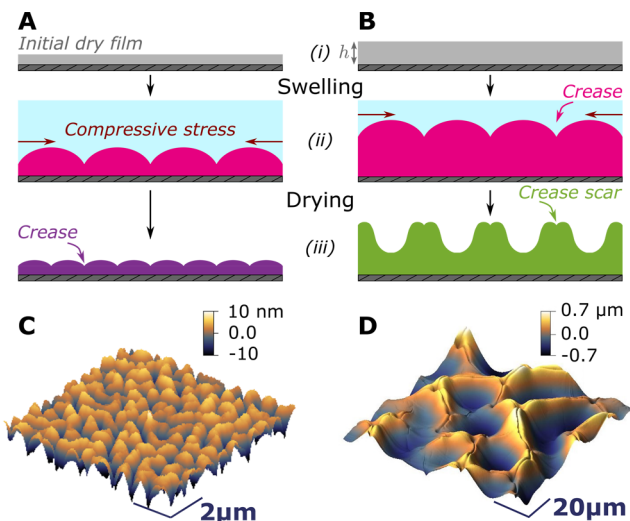


Figure 1. Nanoscale surface patterns in an ultrathin hydrogel films undergoing irreversible swelling/shrinking deformations. A) and B) Schematics of observed patterns, for nanometric (A) and micrometric (B) initial thicknesses. C) and D) 3D reconstruction of the surface topography of two PNIPAM films, with initial dry thicknesses of $h = 232\text{ nm}$ (C) and $h = 4.5\text{ }\mu\text{m}$ (D), that were (i) cross-linked and grafted to a rigid substrate, (ii) swollen by immersion in water, and (iii) dried via evaporation and (C and D) imaged using AFM; colors in C and D correspond to relative surface height (colorbars).

instability occurs at a critical strain threshold of $\epsilon_c \sim 0.30 - 0.35$. We note that this latter threshold is lower than Biot's earlier prediction, suggesting that creases appear before wrinkles as strain increases.^{18,23} The creasing instability is triggered by imperfections, experimentally in the form of nanoscale roughness and numerically by introducing defects.^{4,23,36,37} The singular deformation of a crease requires the bulk elastic energy to overcome the barrier of surface tension. The elastocapillary length $l_{ec} = \gamma/G$ introduces a length scale at which stresses due to the surface tension γ and the shear modulus G are balanced. Creasing thus releases compression, and produces topographic variations that are reminiscent of the structural architecture of the brain,^{22,35,38} and are thus referred to as brain-like in the following. Swelling-induced creases have been observed in many soft and swollen materials^{5,15,17,19,26,27,31,32,39,40} as well as in compressed elastomers^{21,23,41,42} that are thicker than the elastocapillary length. In the latter case, destabilization of the surface is reversible as compression is released. In the following paragraph, we highlight the irreversible character of several swelling-drying processes.

In contrast to swelling matter, drying of complex liquids has been a subject of interest for droplets^{43–46} and films.^{47–50} Drying of solutions found application in the development of the spin-coating technique⁵¹ or in the study of the drying and shrinking of food products.⁵² Deswelling of hydrogels has received less attention in the literature than swelling, and previous studies have focused on macroscopic systems.^{53–55} Although in a drying process the ambient conditions and the initial and final states are precisely reversed compared to swelling, drying is only the reverse process of swelling if it occurs very slowly and if elastic deformations are small with respect to the gel size.⁵³ Nonlinearities that arise through large deformation can render swelling and deswelling as asymmetric processes.^{53,54} These nonlinearities result in nonreciprocal and

irreversible deformations in a single swelling–deswelling cycle.⁵

In particular during swelling, the intake of solvent takes place from the free surface and the swollen hydrogel near the surface thus become more permeable. In contrast, evaporation reduces the fraction of solvent, may even lead to an inhomogeneity of solvent concentration with enhanced polymer concentration at the surface^{43,49,56,57} and thus slower dynamics for the solvent in the near-surface region. The latter phenomenon is reminiscent of the accumulation of solute near the contact line found in drying of thin films of colloidal solutions.^{49,56–58} Phase changes, such as glass transition may occur,^{44,46,48} in a region localized near the surface of polymer films, leading to the formation of a skin layer or “crust”^{46,48,50,59} akin to that seen in drying sessile drops with a pinned contact line.^{44,56,60–63} Buckling instabilities, which are characterized by the whole surface between two pinned lines growing and becoming more curved, have been reported for drying polymer films,^{46,59,64} and colloidal solutions^{64–66} and nonuniform drying may even generate complex structures on dry films such as rings^{67–69} or cracks^{49,70} among other patterns.^{43,60} However, creased patterns on dry films, specifically, have been rarely reported.^{17,71}

Although characteristic features of the creasing instability can be observed in experiments, the mathematical modeling of the phenomenon is challenging. Intrinsic nonlinearity is revealed by the singular shape, then classical linear stability analysis has to be complemented by introducing nucleation and taking into account capillarity in boundary conditions.^{5,16,21,23,37} The latter capillarity involves the effective surface tension between air and the imbibing solvent.⁷² A macroscopic wavelength of instability⁷³ for uniaxial swelling of hydrogels under geometric constraints is identified and roughly scales linearly with the thickness. A finer scaling includes a logarithmic correction, comparing the thickness to the dry elastocapillary length scale l_{ec}^{dry} , given by the ratio between the effective surface tension between the swollen gel and air and the shear modulus of the solid in the initial dry state $l_{ec}^{\text{dry}} = \gamma/G^{\text{dry}}$.^{23,74–76} The model of Dervaux, Ben Amar and Ciarletta^{72,73} is based on the hypotheses that volumetric expansion of the gel associated with swelling is limited by the elasticity of the bulk layer and the surface. Using functional minimization techniques, and imposing a periodic final shape of the surface, they derived the aforementioned scaling with logarithmic correction. This model compares favorably with patterns in swollen films, experimentally performed with an imposed volumetric growth^{3,26–28} and an imposed chemical potential.²⁹

The article is organized as follows: we first describe the sample fabrication and the AFM-based measurement technique. We then investigate typical AFM images of dry and wet PNIPAM films, showing a transition from a creased, brain-like pattern to a more sinusoidal morphology, referred to as volcano-like, and with what we refer to as crease scars. We present a quantitative analysis of these results and discriminate different regimes associated with specific morphologies. We show that hydration-dependent elastic properties determine thresholds for pattern formation. We finally discuss the role evaporation may play in determining the final surface morphology.

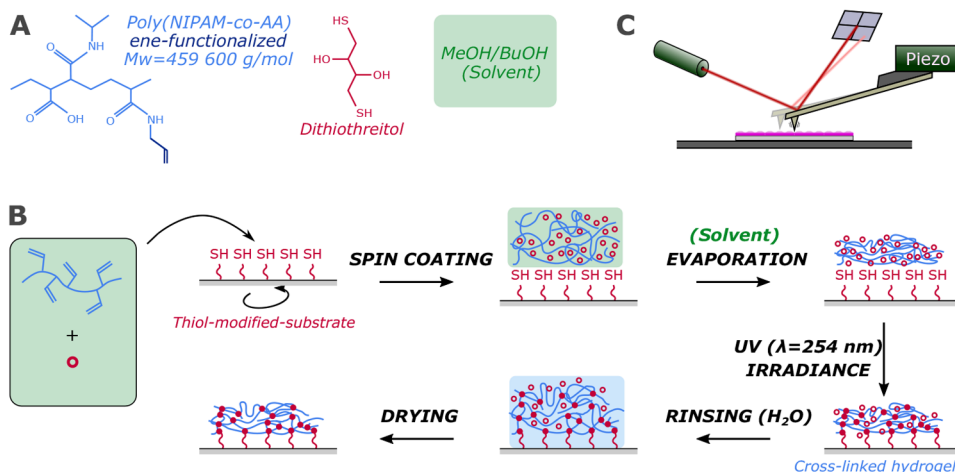


Figure 2. Synthesis by click-chemistry of ultrathin hydrogel films with nanoscale surface patterns. A) P(NIPAM-co-AA) is dissolved in a methanol-butanol mixture (50%/50% in volume) with dithioerythritol, a cross-linker agent. B) Uniform thin films of PNIPAM are achieved through spin-coating and solvent evaporation. The hydrogel films are simultaneously cross-linked and surface-grafted by using thiol–ene click reaction achieved under UV irradiation.^{77–79} Initially flat, dry films are then swollen in water and deswollen via evaporative drying. C) The surface topography of the resulting patterned films is measured using AFM, in both dry and wet conditions. Figure adapted from ref 80, available in Open Access on <https://theses.hal.science/>.

EXPERIMENTS

We prepare PNIPAM surface-grafted hydrogel films using the procedure outlined in Figure 2 (see Section S1.A–D for further details). An in-house synthesized PNIPAM, functionalized with ene-reactive groups (weight-average molar mass $M = 459\,600 \text{ g/mol}$, polydispersity index about 2),^{9,77,78} is used throughout this study. Uniform films of ene-functionalized PNIPAM are produced by spin-coating from a solution onto the surface of thiolated substrates (silicon wafers or glass substrates). Two orders of magnitude variation in film thickness are achieved by spin-coating at different angular velocities, from 1000 to 4000 rpm, and by varying the PNIPAM concentration in the initial polymer solution, from 0.5% to 15% (w/w, see Section S1.C). The hydrogel coating is cross-linked under deep-UV irradiance (see Section S1.D). To remove the excess cross-linker and to induce swelling, samples are immersed in deionized water for 4 h then in isopropanol (HPLC grade) for 15 min. Finally, the samples are dried under ambient conditions.

The surface topography of dry and wet films is measured using an Atomic Force Microscope (Nanosurf CoreAFM). The average thicknesses of dry and wet films are also measured by AFM, after a scalpel is used to cut a line across the dry hydrogel film, exposing the substrate. Finally, the Young's modulus is extracted from AFM force spectroscopy measurements (see Section S3.A).

Several tools were used to rationalize the distinction between brain-like and volcano patterns. In the following, we present these tools and properly define the wavelength λ and amplitude A .

Height Profiles. From an AFM measurement of the surface topography, the height profile along a line is extracted as shown in Figure 3A,B, then a wavelength λ and an amplitude A are computed. For a given image, between 10 and 20 profiles are extracted, and measurements of wavelength and amplitude are averaged. The resulting error on the measured wavelength and amplitude, respectively, is about 5% and 15% or less. This manual method efficiently permits us to distinguish between the pattern types, as the height profiles exhibit different

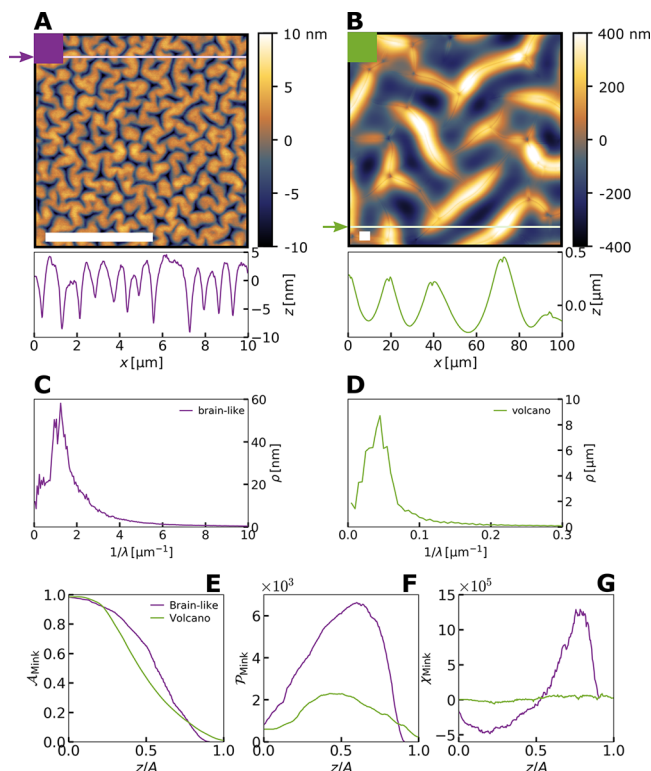


Figure 3. Examples of height profiles, Fourier spectra and Minkowski functionals obtained on typical brain-like (left) and volcano (right) pattern images. A) and B) Typical AFM images and height profile extracted along the indicated line. The white bar represents 5 μm . C) and D) radial averages of 2D Fourier transforms of images showed respectively in panels A) and B). The obtained spectra are showed as a function of the wavenumber $1/\lambda$. Minkowski functionals, calculated from the images showed in panels A) and B). E) Minkowski area $\mathcal{A}_{\text{Mink}}$, F) perimeter $\mathcal{P}_{\text{Mink}}$, and G) connectivity χ_{Mink} measured as a function of height z , normalized by the amplitude of surface topography A .

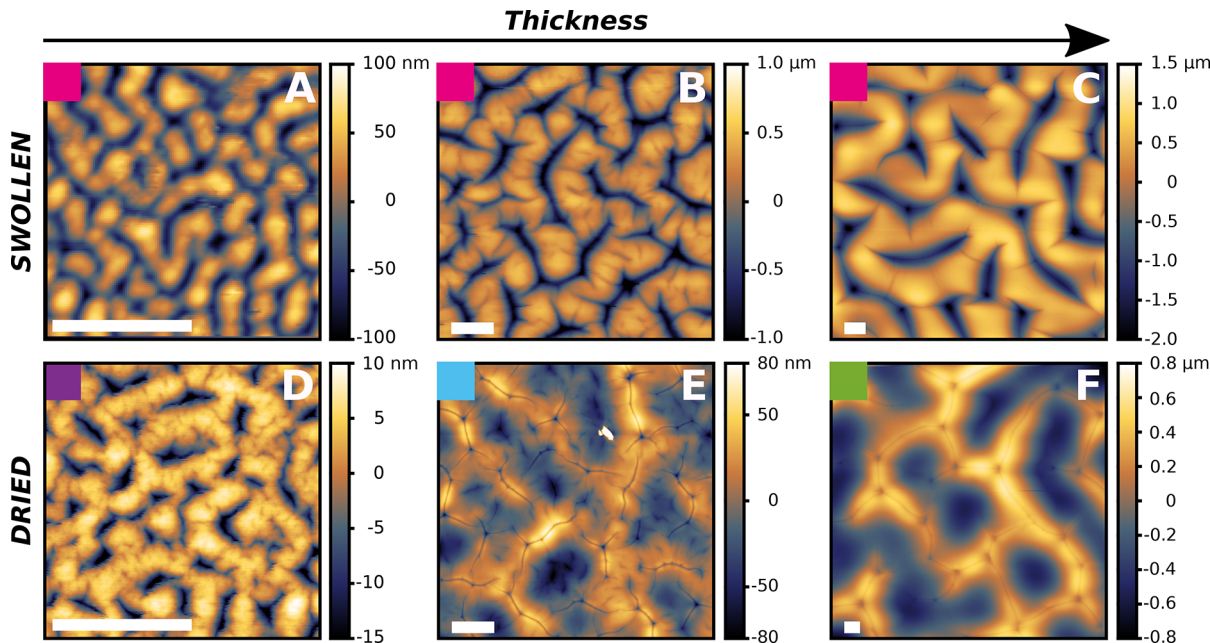


Figure 4. AFM images of dry and wet surface patterns. Top row: swollen state. Bottom row: dry state. Each column represents images of the same sample. The initial thickness h increases from left to right. Left: $h = 320$ nm. Middle: $h = 950$ nm. Right: $h = 4.55 \mu\text{m}$. A–C) Films immersed in water exhibit a brain-like surface patterning. Typical swelling ratio: $S_R = 3.5$. D) Films with initial dry thickness such that $h < l_{\text{ec}}^{\text{wet}}/S_R = \gamma/(G^{\text{wet}} S_R)$ exhibit a brain-like surface patterning. E) An example of the transition regime. F) For dried films with $h > l_{\text{ec}}^{\text{wet}}/S_R$, volcano-like patterns form. White scale bars represent 5 μm for each panel.

features in the cases of brain-like and volcano patterns. Indeed, the height profile extracted from images of samples exhibiting a brain-like pattern (Figure 3A) shows typical creases with steep and discontinuous slopes, while the height profile extracted from images of samples exhibiting a volcano pattern (Figure 3B) appears generally sinusoidal, with smooth valleys and reminiscences of sharp creases on the crests.

Fourier Transform. From the AFM image of a patterned surface, we compute the 2D Fourier transform and perform a radial average of the 2D spectra. In particular, we show in Figure 3C,D the averaged spectra obtained from the typical brain-like and volcano patterns showed in Figure 3A,B. The density ρ is plotted as a function of the wavenumber $1/\lambda$. The wavenumber for which the density reaches a maximum gives a measurement of the dominant wavelength.

The wavelength measurement obtained with the Fourier-based method is consistent with the one obtained with the manual method described above, however the Fourier-based method is less precise. Indeed, a typical image showing patterns with a good resolution usually shows between 5 and 20 spatial periods, which is not enough to precisely compute the Fourier transform.

Minkowski Functionals. From the 3D AFM measurements of the surface topography we compute Minkowski functionals.^{81,82} In particular, the Minkowski area $\mathcal{A}_{\text{Mink}}$, perimeter $\mathcal{P}_{\text{Mink}}$, and connectivity χ_{Mink} were measured as a function of height z (and correspond to the area enclosed by an isocontour, the total length of the isocontours, and number of connected components in an isocontour). Minkowski functionals provide a method of distinguishing 3D patterns with different morphologies⁸³ since morphologically equivalent patterns exhibit the same functional dependence on surface height.

In Figure 3E–G, we show the Minkowski functionals computed from the AFM images showed in Figure 3A,B. The Minkowski functionals clearly demonstrate that the two morphologies are geometrically distinct from one another. For our purposes, the skewness of χ_{Mink} as a function of z/A , as showed in Figure 3G, serves to aid classification of patterns as either brain-like or volcano-like.

In summary, the distinction between pattern types was based on the height profiles, and checked by plotting the Minkowski functionals or simply the height distribution. The measurements of the wavelength and amplitude of the instability were also made from the height profiles analysis.

RESULTS AND DISCUSSION

Results. Typical AFM images of grafted PNIPAM films of different thicknesses are shown in Figure 4: the surface topography and the thickness of three different samples is presented in both wet and dry conditions. During the fabrication process, such patterned morphologies appear only after the first exposition to a solvent rather than during UV irradiance (Figure 2 and see Section S2.A). The first solvent in which swelling occurs and any subsequent drying process selects once and for all the pattern observed after drying. For example, swelling in a second solvent, and repeated swelling and drying cycles, do not change the pattern (see Section S2.B). These observations suggest that surface patterning occurs in our samples as a substrate-attached hydrogel swells due to solvent imbibition, rather than because of a depth-wise gradient in cross-linking density during UV curing.^{5,84–86} While we focus on the dependence of pattern morphology on film thickness, the influence of UV-irradiance time, substrate type, swelling solvent quality and vapor saturation of ambient air were also investigated as detailed in Section S2.B. We observed that the pattern formation was independent of

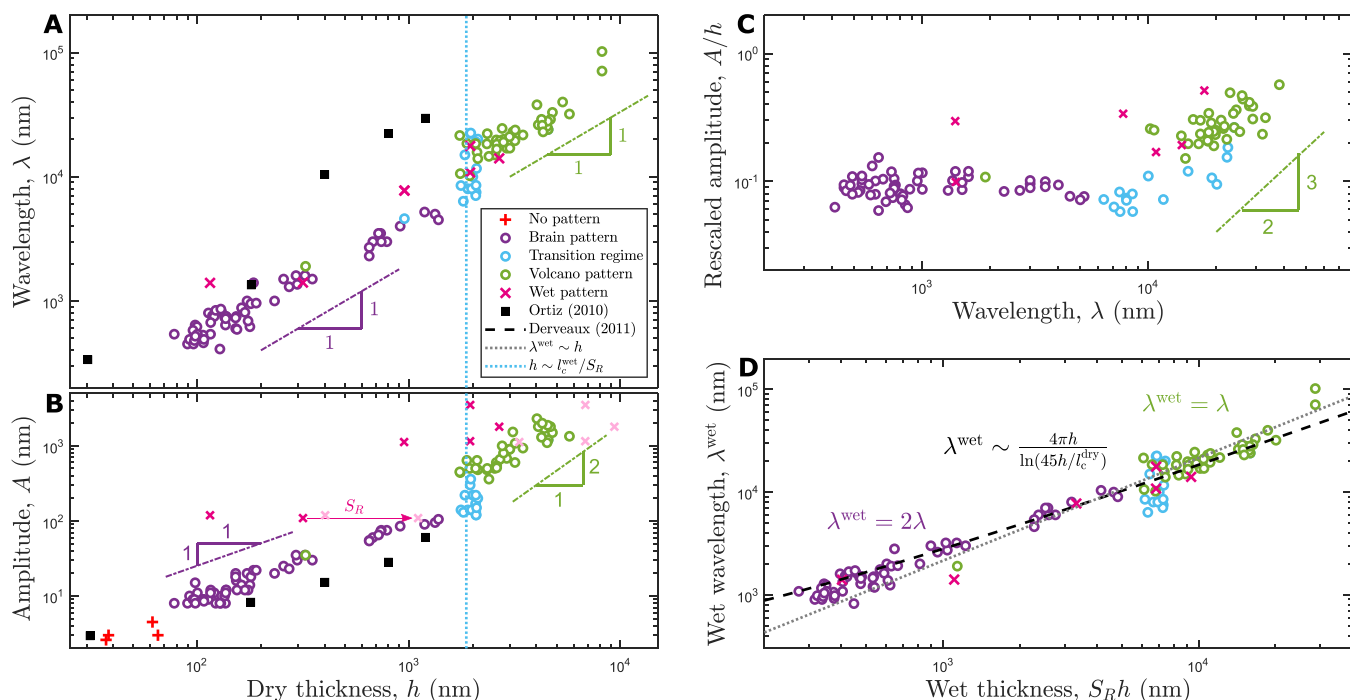


Figure 5. Wavelength and amplitude of surface patterns. A) Wavelength as a function of dry thickness. Different morphologies correspond to different regimes (see color code). The dashed light blue line marks the transition in morphology. The slope triangles indicate power-law exponents. B) Amplitude A as a function of the dry thickness h . Magenta crosses stand for wet amplitude, A , as a function of the dry thickness h . Light pink crosses stand for the amplitude of wet patterns as a function of swollen thickness $S_R h$. The pink arrow represent the shift in thickness induced by the swelling of a factor S_R . C) Amplitude A , scaled by film thickness h , as a function of the wavelength λ . Magenta crosses stand for wet amplitude scaled by the wet thickness $A/(S_R h)$ as a function of wet wavelength λ^{wet} . D) Expected wavelength λ^{wet} when swollen as a function of expected swollen thickness $S_R h$. The black dashed lines represent a linear scaling (dotted line) and the scaling including a logarithmic correction $\lambda^{\text{wet}} \sim 4\pi h / \ln(45h/l_{\text{ec}}^{\text{dry}})$, derived by⁷³ (dashed line). In all, marker colors correspond to pattern types, as indicated in A) except for black squares which correspond to measurements of surface patterns on thin films of block-co-polymer (PNIPAAm-co-MaBP).¹⁷ Figure adapted from ref 80, available in Open Access on <https://theses.hal.science/>.

substrate type (silicon or glass as in Section S1.D). The averaged rinsed-film thickness was independent of UV-irradiance time provided exposure exceeded 1.5 h (see Section S1.D). The influence of the evaporation rate was investigated by saturating the ambient air in water vapor to slow down the evaporation. We observed that slow evaporation did not affect pattern formation (see Section S2.B). Finally, we observed that the shape and amplitude of surface patterns are fixed after the first exposure to a rinsing solvent after UV irradiance. In particular, once formed, patterns are identical upon subsequent swelling-and-drying cycles (see Section S2.A). These observations are consistent with descriptions of swollen gels in literature⁷⁶ and contrast with the one of compressed elastomers which exhibit reversible creases.

Examples of the measured surface patterns shown in Figure 4 evidence a dependence of the surface topography on the initial thickness of the film. The observed surface patterns were classified by morphology as indicated by the colored squares in Figure 4, and detailed in Section S3. Two types of morphology with an intermediate regime are identified. In the case of wet films shown in Figure 4A–C and dried nanometric films in Figure 4D, the surface patterns resemble brain-like patterns. These patterns are typical of a surface-creasing instability found in an elastomer subject to in-plane mechanical compression or a swollen hydrogel.^{3,5,15,17,23,26–30,72,73} The topographies comprise smooth upper peaks separated by sharp plunging creases. The thickest film shown in Figure 4F displays a topography that is distinct from the brain-like pattern, with

broader valleys surrounding sharper peaks. We term this morphology the “volcano” pattern since a small-amplitude crater is observed at the peak summits. Additional images of volcano patterns are shown in Section S2.C.

The average thickness of both wet and dried films was measured. Surface patterns were only observed in dried and wet films with an initial thickness h greater than 70 nm (see Section S2.A). We note that swelling is strongly affected by the surface attachment for ultrathin PNIPAM films.⁹ For films investigated here with $h \gtrsim 150$ nm and 3 h irradiance time, a swelling ratio S_R (i.e. the ratio between the swollen thickness of the hydrated gel and the dry thickness) of about 3.5 was observed. This value of swelling ratio is consistent with results from Li et al.⁹ and corresponds to a mechanical strain $\epsilon = \nu(S_R - 1)$ of about 0.62, taking a Poisson ratio of $\nu = 0.25$ for PNIPAM.^{87,88} Yet, the swelling ratio decreases monotonically with thickness below 150 nm: this suggests that osmotic stress may be insufficient to produce a mechanical strain above the threshold of $\epsilon_c = 0.35$,^{15,16,21,22,35} corresponding to a swelling ratio of 2.4, for creasing in films with a thickness of a few tens of nanometers.

From surface topography measured by AFM, patterns were characterized quantitatively by measuring the wavelength λ and amplitude A as well as the thickness h , in both wet and dry conditions. The wavelength and amplitude of the instability are respectively shown as functions of the initial, dry film thickness in Figure 5A,B. For wet films, the wavelength increases monotonically with the initial, dry thickness. For dried films, a

transition region exists between the two morphological regimes mentioned above. With increasing thickness, the wavelength is multiplied by a factor 2, at a critical thickness that we will discuss in the next section. In the thick-film regime, the wavelength of the wet pattern is comparable to that of the dried pattern, while in the thin-film regime the wavelength of the wet pattern is roughly twice the wavelength of the dried pattern (Figure 5A). The results of Ortiz et al.¹⁷ attained with dried, thin films of PNIPAM copolymerized with methacryloyloxybenzophenone (MaBP), are also included in Figure 5A,B, for reference and are mainly consistent with our results, as we discuss in more detail in the next section.

To characterize the threshold for the formation of volcano patterns on dried films, that marks the transition between the two observed regimes, we measured the material properties of PNIPAM hydrogels in the wet state, using AFM. The Young's modulus in the swollen state was measured to be $E^{\text{wet}} = 35 \pm 5$ kPa (see Section S3.A). This value is larger but on the same order of magnitude than values from literature ($E^{\text{wet}} = 8$ kPa), which may be due to the use of an indentation-based technique.^{12,89} Recalling that the shear modulus is expressed as $G = E/[2(1 + \nu)]$, we then calculated the elastocapillary length $l_{\text{ec}}^{\text{wet}} = \gamma/G^{\text{wet}} = 3.0 \pm 0.5 \mu\text{m}$, with G^{wet} the shear modulus in the wet state. This elastocapillary length is based on wet mechanical properties of PNIPAM. Values were taken from literature for: the surface tension $\gamma = 41.8 \text{ mN/m}$ ⁹⁰ between swollen PNIPAM and air, and the Poisson's ratio $\nu = 0.25$ ^{87,88} of PNIPAM in the swollen state and at room temperature.

Finally, from AFM images presented in Figure 4 the pattern amplitude A was also measured as a function of the initial dry thickness h and is presented in Figure 5B. First, a nanometric surface roughness is measurable as for dried, ultrathin samples that exhibit no pattern. Then for samples thick enough to exhibit a pattern ($h \gtrsim 70 \text{ nm}$), the pattern amplitude of dried films as a function of the initial film thickness switches from a linear behavior to a power law dependency at the same critical thickness as the transition in morphology, as shown in Figure 5B. The result of Ortiz et al. on dried films are included for comparison:¹⁷ the amplitude roughly exhibits the same linear dependency in thickness. The pattern amplitude of wet films as a function of initial film thickness shows at first sight a linear behavior (see Figure 5B, magenta crosses), but swelling induces a prefactor in thickness (see Figure 5B, light pink crosses).

For wet samples, the amplitude as a function of the wet thickness $S_R h$ exhibits a linear scaling, similarly to the amplitude measured on dried brain-like patterns as a function of the initial dry thickness h , and with a similar prefactor. Thus, the ratios between dried or wet amplitude and dried or wet thickness, respectively, appears as a relevant quantity to investigate. In Figure 5C, the ratio between amplitude and film thickness is represented as a function of the wavelength measured on each sample. The ratio between amplitude and initial film thickness shows no dependency on the wavelength for brain-like patterns, while for volcano patterns an increase in a power law is observed, with an approximate 3/2 exponent (Figure 5C). This latter dependency is expected to saturate as the film thickness is increased even further than here, since the pattern amplitude should not become considerably larger than the undisturbed film thickness. Otherwise, more complex

surface patterns such as folds may be observed as was reported elsewhere.^{25,91–94}

From these observations, we conclude that surface creasing results from swelling and the wet-state properties select a particular wavelength of the observed instability. In the case of wet gels, the amplitude of the instability scales with the wet thickness. However, drying may: (i) affect the wavelength, dividing it by a factor two in the case of thin gels, (ii) modify strongly the morphology, and thus the amplitude dependency in the case of thick gels. In the next part, we discuss the thresholds in thickness for the occurrence of patterns observed on dry films, and we speculate on the origins of the morphologies. Furthermore, we compare quantitatively our experimental results on wet films with a theory proposed by Dervaux and Ben Amar.⁷³ Finally, we identify key ingredients and propose a mechanism explaining the emergence of the volcano pattern observed on dry films.

Discussion. Thickness Thresholds for Morphology Change. A threshold thickness of about 70 nm for the creasing instability is observed and was also reported in ref 95 for a given degree of cross-linking. This threshold is related to the thickness-dependent swelling ratio and thus to the volume strain. For these small thicknesses, this swelling-induced strain is not large enough to overcome the subcritical bifurcation inherent to the creasing instability.²² Then, at larger thicknesses, a second threshold thickness of about $h_c \approx 2 \mu\text{m}$ for the formation of the volcano pattern is observed on dried films.

To rationalize this second threshold, we estimate the elastocapillary length based on the mechanical properties of the fully saturated gel, and when the swollen gel dries in contact with ambient air. This length is thus computed to be $l_{\text{ec}}^{\text{wet}} = 3 \mu\text{m}$. The swelling ratio S_R was estimated to be about 3.5 by AFM. Scaled by the swelling ratio, the wet elastocapillary length becomes finally $l_{\text{ec}}^{\text{wet}}/S_R = 0.9 \mu\text{m}$. After drying, the critical initial dry thickness at which the pattern morphology transition, from brain-like to volcanoes, is observed to be $h_c \approx 2 \mu\text{m}$. Taking into account a small overestimation of the Young's modulus due to the indentation measurement technique^{12,89} thus an underestimation of the elastocapillary length, the dry thickness at which the transition occurs is then comparable to the wet elastocapillary length, scaled by the swelling ratio. This suggests that capillary effects indeed play a role in the observed transition. Finally, the results of Ortiz et al.¹⁷ also mention a doubling of the wavelength dependency albeit at a different, yet comparable, critical thickness with our estimate of $l_{\text{ec}}^{\text{wet}}$.

One interpretation of the correspondence between the critical thickness for morphology change and the wet elastocapillary length is as follows. The balance between surface tension and bulk elasticity determines the threshold of the surface (de)stabilization: for wet thicknesses smaller than the wet elastocapillary length, i.e. $h^{\text{wet}} \lesssim l_{\text{ec}}^{\text{wet}}$, surface tension dominates and the surface shape is not significantly affected upon drying, resulting in a creased pattern with a different spacing. For wet thicknesses larger than the wet elastocapillary length, i.e. $h^{\text{wet}} \gtrsim l_{\text{ec}}^{\text{wet}}$, bulk elasticity dominates and the surface shape is destabilized upon drying, leading to the formation of the volcano pattern.

The volcano morphology observed for micrometric, dried films (Figure 4F) is distinct from that previously reported in wet millimetric hydrogels films.^{3,26–29} Indeed, the patterns

previously reported in thick wet hydrogel films are more akin to the brain-like patterns observed in nanometric dried films (Figure 4D). AFM images showing the particular surface shape of the volcano pattern (Figure 4F) are reminiscent of images shown in the work of Ortiz et al.¹⁷ however morphology is not discussed therein. The apparent multiscale patterning observed here is reminiscent of period doubling of wrinkle patterns which typically occur in bilayered systems comprising a thin, prestretched stiff film upon a soft elastomer.^{42,96–103} We are unaware of any description of period doubling or period halving for creases in the literature.

Wavelength Selection. We have discussed the final observed morphologies and their thickness formation threshold. Starting again from the beginning of the process, we now focus on the first swelling phase. We discuss in particular the quantitative measurements of the wavelength as a function of film thickness.

Previous observations of creasing patterns in swollen hydrogel films, similar to our observations of brain-like patterns presented in Figure 4A–C, have been rationalized under the theoretical framework of Dervaux and Ben Amar.⁷³ The wavelength λ^{wet} of the brain-like patterns observed in these swollen, wet systems was found to scale with the initial dry thickness h of the hydrogel: $\lambda^{\text{wet}} \sim 4\pi h / \ln(ah/l_{\text{ec}}^{\text{dry}})$, with $l_{\text{ec}}^{\text{dry}}$ the elastocapillary length computed in the initial dry state and with a numerical prefactor in the natural logarithm $a \approx 45$. This scaling implies that regularization at threshold is done by capillarity in an elastic boundary layer of initial size comparable to the dry elastocapillary length. Experimentally, crease spacings were reported to scale linearly with the thickness.^{17,29,30,95} Indeed, if the threshold for regularization is small compared to the typical sample thickness, a slight deviation from a linear scaling appears in the thinnest samples still exhibiting a pattern.

To compare our data with the model of Dervaux and Ben Amar,⁷³ we first introduce for dried films the wavelength λ^{wet} that is expected in the swollen state, and that was measured for a few samples. For volcano patterns, the measured wavelength in both dried and wet conditions shows no change for a subset of samples, thus we set $\lambda^{\text{wet}} = \lambda$. For dried brain patterns, however, we measure twice the wavelength of the dried state in the swollen state (see magenta crosses in Figure 5A), thus we set $\lambda^{\text{wet}} = 2\lambda$, where the factor of 2 was verified to be the best fitting value, within 2% error. The wet wavelength λ^{wet} is represented as a function of the swollen thickness $S_R h$ in Figure 5D, and shows a small deviation from a linear behavior.

The slight sublinear behavior is captured by the model of Dervaux and Ben Amar: a fit of the data with the scaling including a logarithmic correction results in an estimation of the dry elastocapillary length of $l_{\text{ec}}^{\text{dry}} \approx 150$ nm and a corresponding shear modulus of $G^{\text{dry}} \approx 280$ kPa (see Section. S3.B for the estimate precision). This estimation of shear modulus, which lies between the glassy and fully swollen ones measured here (Section. S3.A), is a value that the modulus could take after enough solvent is absorbed by the gel to cross the glass-to-rubber transition. In summary, with our expectation of wavelength λ^{wet} in the swollen state, our data for dried samples show an excellent agreement with the theoretical prediction of Dervaux and Ben Amar.⁷³ We propose the following interpretation: the geometrical expansion due to swelling is large enough to overcome the surface tension,⁷⁵

In the two previous paragraphs, we rationalized the wavelength measurements of different pattern types in the dry state by linking them with patterns observed in the wet state. Based on these observations, we conclude that the wavelength is set in the wet state, as a result of swelling. In the next paragraphs we examine how the evolution of the pattern shape during drying may proceed.

Morphological Evolution Upon Drying. As liquid evaporates out of the gel, the film passes through a rubber-to-glass transition triggered by dehydration, when the polymer concentration is large enough.^{104,105} Since evaporation takes place from the free surface, at a critical solvent fraction a glassy skin layer is formed.^{106–108} This skin layer first increases in thickness rapidly, and then expands with a diffusive dynamics.¹⁰⁸ In our situation, the initial condition for drying of the swollen hydrogel films is not a flat free surface, as is the common case described in ref 50. Instead, the formation of the glassy skin layer due to evaporation takes place from an initially creased surface. We now focus on how such creasing could affect the spatial distribution of polymer within the film at the onset of evaporation. We separate the two different thickness regimes in terms of the elastocapillary length estimated above.

In the first case $h \lesssim l_{\text{ec}}^{\text{wet}}/S_R$, surface tension effects dominate elastic stresses in the soft and swollen gel, smoothing out large-curvature features in the gel. In this regime, a drying front propagates in time, yet the film is thin enough to dry uniformly. In this situation, smaller-wavelength creases become more geometrically favorable as the scaling argument predicts $\lambda \sim h$.⁷³ However, a wavelength was already selected during swelling (Figure 1, first column). Following drying, we observe a new wavelength emerging with half the period. The fact that the emergent wavelength is an integer fraction of the pre-existing crease in the swollen state suggests that periodicity is preserved during drying, i.e. the shape of the surface instability is constrained by the spatial distribution of the preexisting creases. It seems reasonable that either the glass transition, or a crossover into the nonincreasing regime of solvent fraction, is reached before a further wavelength reduction could be affected.

In a second case for films with $h \gtrsim l_{\text{ec}}^{\text{wet}}/S_R$, we propose the following mechanism. Bulk elasticity coming from the swollen gel underneath the surface dominates over surface tension. As the gel dries, a glassy skin layer forms initially at the surface and then expands in time.¹⁰⁸ The skin layer is stiffer than the still-hydrated gel underneath, by up to 4 orders of magnitude (see Section. S3.A for the Young's modulus measurements). Additionally, as drying generates a loss of solvent, the stiff crust would shrink, generating in-plane compressive stresses. Such stresses would pull the surface of the still-hydrated swollen gel underneath. In such a situation, a stretched, stiff and thin layer exists on a thick and soft material. Numerous works have showed that a wrinkling instability can thus appear once a critical compressive strain is exceeded.^{25,38,42,92,109–117} The surface of the bilayer becomes destabilized, taking a sinusoidal shape, whose wavelength scales as $\lambda \sim (t_s H)^{1/2} (E_s/E)^{1/6}$, with t_s and H the thicknesses, E_s and E the Young's moduli of the skin and the substrate, respectively. In our case, a wrinkling instability could thus appear on an initially creased surface, with the spatial distribution of solvent and wavelength of wrinkles preselected by the creases in the swollen film.

We estimate the thickness of the skin layer at the moment when the critical strain is exceeded using the wavelength of the

crease pattern, $t_s \sim (\lambda^2/H)(E/E_s)^{1/3}$. We find it to be approximately 7% of the swollen thickness of the film, using $E = E^{\text{wet}} = 35\text{kPa}$ and $E_s = E^{\text{dry}} = 700\text{ MPa}$ (see Section S3.A), which is expected to be reached almost instantaneously once the formation of the skin layer is initiated.¹⁰⁸ By opposition to the depth of creases and because of the extreme curvature in the region of the creases,¹¹⁸ the bumped regions are less constrained and thus shrink more during evaporation. Such shrinking may also occur preferentially from the peaks of the bumps than in the vicinity of the creases,¹¹⁹ possibly creating an inversion of the topography. Indeed we observe the resulting surface morphology to be characterized by a globally sinusoidal profile, with scars of creases present at the crests. Thus, the wavelength of the dried volcano pattern is prescribed by the swollen creased patterns initiated in the wet state.

In summary, swelling and drying hydrogels may experience elastic instabilities that affect the surface topography. During swelling the originally flat surface is deformed by an in-plane compressive stress, resulting in the formation of creases. During drying, depending on the balance between surface tension and bulk elasticity, the formation of a thin, stiff and glassy skin layer on the still-hydrated and soft gel may significantly affect the final surface morphology of the dried film. The final surface morphology of dried films can therefore be a brain-like or a volcano pattern and is determined by this drying process, depending on the thickness of the wet film before drying commences.

CONCLUSIONS

We have investigated the irreversible deformation of grafted PNIPAM films, of nanometric and micrometric thickness, caused by imbibition-induced swelling and evaporation-driven shrinking. Relatively thin, nanometric films undergo a swelling instability that leads to a brain-like pattern, typical of surface creasing instabilities and with a set spacing. When drying, the surface morphology keeps the creased shape although the spatial frequency of creases is doubled as compared to the wet state. The new pattern is then locked-in as the film shrinks (through the glass transition) into a dried film. The typical amplitude of these surface patterns with submicrometric wavelengths ($\lambda \leq 1\text{ }\mu\text{m}$) is consistently $\sim 10\%$ of the film thickness, independent of the wavelength (see Figure 5C). Thicker, micrometric films also develop surface creases because of in-plane compressive forces that result from constrained swelling due to surface attachment. However, drying is known to induce the formation of a glassy skin layer. We propose that this glassy layer is responsible for a subsequent change in topographic morphology, rendering it distinct from the brain-like pattern observed in the wet state.

ASSOCIATED CONTENT

S Supporting Information

The Supporting Information is available free of charge at <https://pubs.acs.org/doi/10.1021/acs.langmuir.4c04025>.

Additional experimental details, materials, methods, and peripheral observations (PDF)

The reported experimental data (ZIP)

AUTHOR INFORMATION

Corresponding Authors

Finn Box – Gulliver, CNRS, ESPCI Paris and Institut Pierre Gilles de Gennes (IPGG), ESPCI Paris, Université PSL, Paris 75005, France; Physics of Fluids & Soft Matter, Department of Physics & Astronomy, University of Manchester, Manchester M13 9PL, U.K.; Email: finn.box@manchester.ac.uk

Joshua D. McGraw – Gulliver, CNRS, ESPCI Paris and Institut Pierre Gilles de Gennes (IPGG), ESPCI Paris, Université PSL, Paris 75005, France; orcid.org/0000-0003-4925-5496; Email: joshua.mcgraw@espci.fr

Authors

Caroline Kopecz-Muller – Gulliver, CNRS, ESPCI Paris and Institut Pierre Gilles de Gennes (IPGG), ESPCI Paris, Université PSL, Paris 75005, France; Univ. Bordeaux, CNRS, LOMA, UMR 5798, Talence F-33400, France

Clemence Gaunand – Gulliver, CNRS, ESPCI Paris and Institut Pierre Gilles de Gennes (IPGG), ESPCI Paris, Université PSL, Paris 75005, France

Yvette Tran – Sciences et Ingénierie de la Matière Molle, CNRS, ESPCI Paris, Université PSL, 75005 Paris, France; Sorbonne-Universités, UPMC Université Paris 06, Paris 75005, France

Matthieu Labousse – Gulliver, CNRS, ESPCI Paris, Université PSL, Paris 75005, France

Elie Raphaël – Gulliver, CNRS, ESPCI Paris, Université PSL, Paris 75005, France

Thomas Salez – Univ. Bordeaux, CNRS, LOMA, UMR 5798, Talence F-33400, France; orcid.org/0000-0001-6111-8721

Complete contact information is available at:
<https://pubs.acs.org/10.1021/acs.langmuir.4c04025>

Funding

The authors acknowledge financial support from the CNRS, and from the Agence Nationale de la Recherche (ANR) under the CoPinS (ANR-19-CE06-0021), Softer (ANR-21-CE06-0029), and Fricolas (ANR-21-CE06-0039) grants, the Institut Pierre-Gilles de Gennes (Equipex ANR-10-EQPX-34 and Labex ANR-10-LABX-31) and PSL Research University (Idex ANR-10-IDEX-0001-02). They also acknowledge support from the European Union through the European Research Council under EMetBrown (ERC-CoG-101039103) grant. Views and opinions expressed are however those of the authors only and do not necessarily reflect those of the European Union or the European Research Council. Neither the European Union nor the granting authority can be held responsible for them. They finally acknowledge the Royal Society (URF/R1/211730).

Notes

The authors declare no competing financial interest.

ACKNOWLEDGMENTS

The authors are more than grateful to Marjan Abdorahim for sharing her strong expertise on hydrogels. The authors gratefully acknowledge Patrick Tabeling, Ousmane Kodio, Ken Sekimoto, Grae Worster, Joseph Webber, Noushine Shahidzadeh and Romane Le Dizès Castell for insightful comments and fruitful discussions. The AFM work benefited from EUSMI TA support and expertise of Dr. Peisker from

Nanosurf. The experimental work benefited from the technical contribution of the joint service unit CNRS UAR 3750. Finally, the authors thank the Soft Matter Collaborative Research Unit, Frontier Research Center for Advanced Material and Life Science, Faculty of Advanced Life Science at Hokkaido University, Sapporo, Japan.

■ REFERENCES

- (1) Russell, T. P. Surface-Responsive Materials. *Science* **2002**, *297*, 964–967.
- (2) Ahn, S.-K.; Kasi, R. M.; Kim, S.-C.; Sharma, N.; Zhou, Y. Stimuli-responsive polymer gels. *Soft Matter* **2008**, *4*, 1151–1157.
- (3) Li, C.; Hu, Z.; Li, Y. Temperature and time dependencies of surface patterns in constrained ionic N-isopropylacrylamide gels. *J. Chem. Phys.* **1994**, *100*, 4645–4652.
- (4) Kim, J.; Yoon, J.; Hayward, R. C. Dynamic display of biomolecular patterns through an elastic creasing instability of stimuli-responsive hydrogels. *Nat. Mater.* **2010**, *9*, 159–164.
- (5) Yoon, J.; Kim, J.; Hayward, R. C. Nucleation, growth, and hysteresis of surface creases on swelled polymer gels. *Soft Matter* **2010**, *6*, 5807–5816.
- (6) Beebe, D.; Moore, J.; Bauer, J.; Yu, Q.; Liu, R. H.; Devadoss, C.; Jo, B.-H. Free-evolution kinetics in a high-swelling polymeric hydrogel. *Nature* **2000**, *404*, 588–590.
- (7) Idota, N.; Kikuchi, A.; Kobayashi, J.; Sakai, K.; Okano, T. Microfluidic Valves Comprising Nanolayered Thermoresponsive Polymer-Grafted Capillaries. *Adv. Mater.* **2005**, *17*, 2723–2727.
- (8) D'Eramo, L.; Chollet, B.; Leman, M.; Martwong, E.; Li, M.; Geisler, H.; Dupire, J.; Kerdraon, M.; Vergne, C.; Monti, F.; et al. Microfluidic actuators based on temperature-responsive hydrogels. *Microsyst. Nanoeng.* **2018**, *4*, 17069.
- (9) Li, M.; Bresson, B.; Cousin, F.; Fréaigny, C.; Tran, Y. Submicrometric Films of Surface-Attached Polymer Network with Temperature-Responsive Properties. *Langmuir* **2015**, *31*, 11516–11524.
- (10) Winnik, F. M. Fluorescence studies of aqueous solutions of poly (N-isopropylacrylamide) below and above their LCST. *Macromolecules* **1990**, *23*, 233–242.
- (11) Heskins, M.; Guillet, J. E. Solution properties of poly (N-isopropylacrylamide). *J. Macromol. Sci., Chem.* **1968**, *2*, 1441–1455.
- (12) Haq, M. A.; Su, Y.; Wang, D. Mechanical properties of PNIPAM based hydrogels: A review. *Mater. Sci. Eng., C* **2017**, *70*, 842–855.
- (13) Peppas, N.; Hilt, J.; Khademhosseini, A.; Langer, R. Hydrogels in Biology and Medicine: From Molecular Principles to Bionanotechnology. *Adv. Mater.* **2006**, *18*, 1345–1360.
- (14) Eslahi, N.; Abdorahim, M.; Simchi, A. Smart Polymeric Hydrogels for Cartilage Tissue Engineering: A Review on the Chemistry and Biological Functions. *Biomacromolecules* **2016**, *17*, 3441–3463.
- (15) Trujillo, V.; Kim, J.; Hayward, R. C. Creasing instability of surface-attached hydrogels. *Soft Matter* **2008**, *4*, 564–569.
- (16) Hong, W.; Zhao, X.; Suo, Z. Formation of creases on the surfaces of elastomers and gels. *Appl. Phys. Lett.* **2009**, *95*, 111901.
- (17) Ortiz, O.; Vidyasagar, A.; Wang, J.; Toomey, R. Surface Instabilities in Ultrathin, Cross-Linked Poly(N-isopropylacrylamide) Coatings. *Langmuir* **2010**, *26*, 17489–17494.
- (18) Chen, D.; Yoon, J.; Chandra, D.; Crosby, A. J.; Hayward, R. C. Stimuli-responsive buckling mechanics of polymer films. *J. Polym. Sci., Part B: Polym. Phys.* **2014**, *52*, 1441–1461.
- (19) Ju, J.; Sekimoto, K.; Cipelletti, L.; Creton, C.; Narita, T. Heterogeneous nucleation of creases in swelling polymer gels. *Phys. Rev. E* **2022**, *105*, 034504.
- (20) Ciarletta, P. Matched asymptotic solution for crease nucleation in soft solids. *Nat. Commun.* **2018**, *9*, 496.
- (21) Cai, S.; Chen, D.; Suo, Z.; Hayward, R. C. Creasing instability of elastomer films. *Soft Matter* **2012**, *8*, 1301–1304.
- (22) Hohlfeld, E.; Mahadevan, L. Unfolding the Sulcus. *Phys. Rev. Lett.* **2011**, *106*, 105702.
- (23) Chen, D.; Cai, S.; Suo, Z.; Hayward, R. C. Surface Energy as a Barrier to Creasing of Elastomer Films: An Elastic Analogy to Classical Nucleation. *Phys. Rev. Lett.* **2012**, *109*, 038001.
- (24) Suematsu, N.; Sekimoto, K.; Kawasaki, K. Three-dimensional computer modeling for pattern formation on the surface of an expanding polymer gel. *Phys. Rev. A* **1990**, *41*, 5751–5754.
- (25) Li, B.; Cao, Y.-P.; Feng, X.-Q.; Gao, H. Mechanics of morphological instabilities and surface wrinkling in soft materials: A review. *Soft Matter* **2012**, *8*, 5728–5745.
- (26) Tanaka, T.; Sun, S.-T.; Hirokawa, Y.; Katayama, S.; Kucera, J.; Hirose, Y.; Amiya, T. Mechanical instability of gels at the phase transition. *Nature* **1987**, *325*, 796–798.
- (27) Tanaka, H.; Tomita, H.; Takasu, A.; Hayashi, T.; Nishi, T. Morphological and kinetic evolution of surface patterns in gels during the swelling process: Evidence of dynamic pattern ordering. *Phys. Rev. Lett.* **1992**, *68*, 2794–2797.
- (28) Li, Y.; Li, C.; Hu, Z. Pattern formation of constrained acrylamide/sodium acrylate copolymer gels in acetone/water mixture. *J. Chem. Phys.* **1994**, *100*, 4637–4644.
- (29) Gérardin, H.; Buguin, A.; Brochard-Wyart, F. *Pattern formation in anti-fog and anti-frost polymer coatings*, Ph.D. thesis, Institut Curie, 2006.
- (30) Durie, K.; Razavi, M. J.; Wang, X.; Locklin, J. Nanoscale Surface Creasing Induced by Post-polymerization Modification. *ACS Nano* **2015**, *9*, 10961–10969.
- (31) Sheppard, S. E.; Elliott, F. A. The Reticulation of Gelatine. *J. Ind. Eng. Chem.* **1918**, *10*, 727–732.
- (32) Southern, E.; Thomas, A. Effect of constraints on the equilibrium swelling of rubber vulcanizates. *J. Polym. Sci., Part A: Gen. Pap.* **1965**, *3*, 641–646.
- (33) Biot, M. A. SURFACE INSTABILITY OF RUBBER IN COMPRESSION. *Appl. Sci. Res. A* **1963**, *12*, 168–182.
- (34) Mora, S.; Abkarian, M.; Tabuteau, H.; Pomeau, Y. Surface instability of soft solids under strain. *Soft Matter* **2011**, *7*, 10612–10619.
- (35) Hohlfeld, E. B. *Creasing, point-bifurcations, and the spontaneous breakdown of scale-invariance*; Ph.D. Thesis Harvard University, 2008.
- (36) Cao, Y.; Hutchinson, J. W. From wrinkles to creases in elastomers: The instability and imperfection-sensitivity of wrinkling. *Proc. R. Soc. London, Ser. A* **2012**, *468*, 94–115.
- (37) Wong, W.; Guo, T.; Zhang, Y.; Cheng, L. Surface instability maps for soft materials. *Soft Matter* **2010**, *6*, 5743–5750.
- (38) Tallinen, T.; Biggins, J. S.; Mahadevan, L. Surface Sulci in Squeezed Soft Solids. *Phys. Rev. Lett.* **2013**, *110*, 024302.
- (39) Guvendiren, M.; Burdick, J. A.; Yang, S. Solvent induced transition from wrinkles to creases in thin film gels with depth-wise crosslinking gradients. *Soft Matter* **2010**, *6*, 5795–5801.
- (40) Drummond, W. R.; Knight, M. L.; Brannon, M. L.; Peppas, N. A. Surface instabilities during swelling of pH-sensitive hydrogels. *J. Controlled Release* **1988**, *7*, 181–183.
- (41) Ghatak, A.; Das, A. L. Kink instability of a highly deformable elastic cylinder. *Phys. Rev. Lett.* **2007**, *99*, 076101.
- (42) Chen, D.; Jin, L.; Suo, Z.; Hayward, R. C. Controlled formation and disappearance of creases. *Mater. Horiz.* **2014**, *1*, 207–213.
- (43) Deegan, R. D. Pattern formation in drying drops. *Phys. Rev. E* **2000**, *61*, 475.
- (44) Zang, D.; Tarafdar, S.; Tarasevich, Y. Y.; Choudhury, M. D.; Dutta, T. Evaporation of a Droplet: From physics to applications. *Phys. Rep.* **2019**, *804*, 1–56.
- (45) Ozawa, K.; Nishitani, E.; Doi, M. Modeling of the drying process of liquid droplet to form thin film. *Jpn. J. Appl. Phys.* **2005**, *44*, 4229.
- (46) Pauchard, L.; Allain, C. Stable and unstable surface evolution during the drying of a polymer solution drop. *Phys. Rev. E* **2003**, *68*, 052801.

- (47) De Gennes, P.-G. Instabilities during the evaporation of a film: Non-glassy polymer+ volatile solvent. *Eur. Phys. J. E* **2001**, *6*, 421–424.
- (48) De Gennes, P.-G. Solvent evaporation of spin cast films: “crust” effects. *Eur. Phys. J. E* **2002**, *7*, 31–34.
- (49) Routh, A. F. Drying of thin colloidal films. *Rep. Prog. Phys.* **2013**, *76*, 046603.
- (50) Okuzono, T.; Ozawa, K.; Doi, M. Simple model of skin formation caused by solvent evaporation in polymer solutions. *Phys. Rev. Lett.* **2006**, *97*, 136103.
- (51) Bornside, D.; Macosko, C.; Scriven, L. Spin coating: One-dimensional model. *J. Appl. Phys.* **1989**, *66*, 5185–5193.
- (52) Fu, N.; Yu, M.; Chen, X. D. A differential shrinkage approach for evaluating particle formation behavior during drying of sucrose, lactose, mannitol, skim milk, and other solid-containing droplets. *Dry. Technol.* **2019**, *37*, 941–949.
- (53) Bertrand, T.; Peixinho, J.; Mukhopadhyay, S.; MacMinn, C. W. Dynamics of Swelling and Drying in a Spherical Gel. *Phys. Rev. Appl.* **2016**, *6*, 064010.
- (54) Etzold, M. A.; Linden, P. F.; Worster, M. G. Transpiration through hydrogels. *J. Fluid Mech.* **2021**, *925*, A8.
- (55) Engelsberg, M.; Barros, W. Free-evolution kinetics in a high-swelling polymeric hydrogel. *Phys. Rev. E* **2013**, *88*, 062602.
- (56) Deegan, R. D.; Bakajin, O.; Dupont, T. F.; Huber, G.; Nagel, S. R.; Witten, T. A. Contact line deposits in an evaporating drop. *Phys. Rev. E* **2000**, *62*, 756.
- (57) Hennessy, M. G.; Ferretti, G. L.; Cabral, J. T.; Matar, O. K. A minimal model for solvent evaporation and absorption in thin films. *J. Colloid Interface Sci.* **2017**, *488*, 61–71.
- (58) Deegan, R. D.; Bakajin, O.; Dupont, T. F.; Huber, G.; Nagel, S. R.; Witten, T. A. Capillary flow as the cause of ring stains from dried liquid drops. *Nature* **1997**, *389*, 827–829.
- (59) Pauchard, L.; Allain, C. Buckling instability induced by polymer solution drying. *Europhys. Lett.* **2003**, *62*, 897.
- (60) Larson, R. G. Transport and deposition patterns in drying sessile droplets. *AIChE J.* **2014**, *60*, 1538–1571.
- (61) Hu, H.; Larson, R. G. Analysis of the microfluid flow in an evaporating sessile droplet. *Langmuir* **2005**, *21*, 3963–3971.
- (62) Hu, H.; Larson, R. G. Analysis of the effects of Marangoni stresses on the microflow in an evaporating sessile droplet. *Langmuir* **2005**, *21*, 3972–3980.
- (63) Pouillard, C.; Damman, P. Control of spreading and drying of a polymer solution from Marangoni flows. *Europhys. Lett.* **2007**, *80*, 64001.
- (64) Pauchard, L.; Allain, C. Mechanical instability induced by complex liquid desiccation. *C. R. Phys.* **2003**, *4*, 231–239.
- (65) Zhou, J.; Man, X.; Jiang, Y.; Doi, M. Structure Formation in Soft-Matter Solutions Induced by Solvent Evaporation. *Adv. Mater.* **2017**, *29*, 1703769.
- (66) Vermant, J.; Solomon, M. J. Flow-induced structure in colloidal suspensions. *J. Condens. Matter Phys.* **2005**, *17*, R187.
- (67) Chen, L.; Evans, J. R. Arched structures created by colloidal droplets as they dry. *Langmuir* **2009**, *25*, 11299–11301.
- (68) McGraw, J. D.; Li, J.; Tran, D. L.; Shi, A.-C.; Dalnoki-Veress, K. Plateau-Rayleigh instability in a torus: Formation and breakup of a polymer ring. *Soft Matter* **2010**, *6*, 1258–1262.
- (69) McGraw, J. D.; Rowe, I. D. W.; Matsen, M. W.; Dalnoki-Veress, K. Dynamics of interacting edge defects in copolymer lamellae. *Eur. Phys. J. E* **2011**, *34*, 131.
- (70) Xie, K.; Glasser, A.; Shinde, S.; Zhang, Z.; Ramponoux, J.-M.; Maali, A.; Cloutet, E.; Hadzioannou, G.; Kellay, H. Delamination and wrinkling of flexible conductive polymer thin films. *Adv. Funct. Mater.* **2021**, *31*, 2009039.
- (71) Saintyves, B.; Pic, R.; Mahadevan, L.; Bischofberger, I. Evaporation-Driven Cellular Patterns in Confined Hyperelastic Hydrogels. *Phys. Rev. Lett.* **2023**, *131*, 118202.
- (72) Ben Amar, M.; Ciarletta, P. Swelling Instability of surface-attached gels as a model of soft tissue growth under geometric constraints. *J. Mech. Phys. Solids* **2010**, *58*, 935–954.
- (73) Dervaux, J.; Ben Amar, M. Buckling condensation in constrained growth. *J. Mech. Phys. Solids* **2011**, *59*, 538–560.
- (74) Kang, M. K.; Huang, R. Swell-induced surface instability of confined hydrogel layers on substrates. *J. Mech. Phys. Solids* **2010**, *58*, 1582–1598.
- (75) Liu, Q.; Ouchi, T.; Jin, L.; Hayward, R.; Suo, Z. Elastocapillary Crease. *Phys. Rev. Lett.* **2019**, *122*, 098003.
- (76) van Limbeek, M. A. J.; Essink, M. H.; Pandey, A.; Snoeijer, J. H.; Karpitschka, S. Pinning-Induced Folding-Unfolding Asymmetry in Adhesive Creases. *Phys. Rev. Lett.* **2021**, *127*, 028001.
- (77) Chollet, B.; D'eraimo, L.; Martwong, E.; Li, M.; Macron, J.; Mai, T. Q.; Tabeling, P.; Tran, Y. Tailoring patterns of surface-attached multiresponsive polymer networks. *ACS Appl. Mater. Interfaces* **2016**, *8*, 24870–24879.
- (78) Benjamin, C.; Mengxing, L.; Ekkachai, M.; Bruno, B.; Christian, F.; Patrick, T.; Yvette, T. Multiscale Surface-Attached Hydrogel Thin Films with Tailored Architecture. **2016**.
- (79) Kolb, H. C.; Finn, M.; Sharpless, K. B. Click chemistry: Diverse chemical function from a few good reactions. *Angew. Chem., Int. Ed.* **2001**, *40*, 2004–2021.
- (80) Kopecz-Muller, C. *Mechanics of hydrogel films: Swelling-induced instabilities, finite-size effects, and contactless rheology to indentation-induced dehydration*. Ph.D. thesis, Université de Bordeaux, 2024.
- (81) Mecke, K. R. Integral Geometry in Statistical Physics. *Int. J. Modern Phys. B* **1998**, *12*, 861–899.
- (82) Fetzer, R.; Rauscher, M.; Seemann, R.; Jacobs, K.; Mecke, K. Thermal Noise Influences Fluid Flow in Thin Films during Spinodal Dewetting. *Phys. Rev. Lett.* **2007**, *99*, 114503.
- (83) Scholz, C.; Schröder-Turk, G. E.; Mecke, K. Pattern-fluid interpretation of chemical turbulence. *Phys. Rev. E* **2015**, *91*, 042907.
- (84) Yang, S.; Khare, K.; Lin, P.-C. Harnessing Surface Wrinkle Patterns in Soft Matter. *Adv. Funct. Mater.* **2010**, *20*, 2550–2564.
- (85) Chandra, D.; Crosby, A. Self-Wrinkling of UV-Cured Polymer Films. *Adv. Mater.* **2011**, *23*, 3441–3445.
- (86) Um, E.; Cho, Y.-K.; Jeong, J. Spontaneous Wrinkle Formation on Hydrogel Surfaces Using Photoinitiator Diffusion from Oil-Water Interface. *ACS Appl. Mater. Interfaces* **2021**, *13*, 15837–15846.
- (87) Hirotsu, S. Softening of bulk modulus and negative Poisson's ratio near the volume phase transition of polymer gels. *J. Chem. Phys.* **1991**, *94*, 3949–3957.
- (88) Boon, N.; Schurtenberger, P. Swelling of micro-hydrogels with a crosslinker gradient. *Phys. Chem. Chem. Phys.* **2017**, *19*, 23740–23746.
- (89) Hashmi, S. M.; Dufresne, E. R. Mechanical properties of individual microgel particles through the deswelling transition. *Soft Matter* **2009**, *5*, 3682–3688.
- (90) Zhang, J.; Pelton, R. The surface tension of aqueous poly(N-isopropylacrylamide-co-acrylamide). *J. Polymer Sci. A* **1999**, *37*, 2137–2143.
- (91) Kim, P.; Abkarian, M.; Stone, H. Hierarchical folding of elastic membranes under biaxial compressive stress. *Nat. Mater.* **2011**, *10*, 952–957.
- (92) Pocivavsek, L.; Dellsy, R.; Kern, A.; Johnson, S.; Lin, B.; Lee, K. Y. C.; Cerda, E. Stress and fold localization in thin elastic membranes. *Science* **2008**, *320*, 912–916.
- (93) Oshri, O.; Diamant, H. Pattern transitions in a compressible floating elastic sheet. *Phys. Chem. Chem. Phys.* **2017**, *19*, 23817–23824.
- (94) Diamant, H.; Witten, T. A. Compression induced folding of a sheet: An integrable system. *Phys. Rev. Lett.* **2011**, *107*, 164302.
- (95) Hayward, R. C.; Chmelka, B. F.; Kramer, E. J. Template Cross-Linking Effects on Morphologies of Swellable Block Copolymer and Mesostructured Silica Thin Films. *Macromolecules* **2005**, *38*, 7768–7783.
- (96) Bowden, N.; Huck, W. T. S.; Paul, K. E.; Whitesides, G. M. The controlled formation of ordered, sinusoidal structures by plasma oxidation of an elastomeric polymer. *Appl. Phys. Lett.* **1999**, *75*, 2557–2559.

- (97) Yoo, P. J.; Lee, H. H. Evolution of a stress-driven pattern in thin bilayer films: Spinodal wrinkling. *Phys. Rev. Lett.* **2003**, *91*, 154502.
- (98) Harrison, C.; Stafford, C. M.; Zhang, W.; Karim, A. Sinusoidal phase grating created by a tunably buckled surface. *Appl. Phys. Lett.* **2004**, *85*, 4016–4018.
- (99) Stafford, C. M.; Vogt, B. D.; Harrison, C.; Julthongpiput, D.; Huang, R. Elastic Moduli of Ultrathin Amorphous Polymer Films. *Macromolecules* **2006**, *39*, 5095–5099.
- (100) Brau, F.; Vandeparre, H.; Sabbah, A.; Pouillard, C.; Boudaoud, A.; Damman, P. Multiple-length-scale elastic instability mimics parametric resonance of nonlinear oscillators. *Nat. Phys.* **2011**, *7*, 56–60.
- (101) Huntington, M. D.; Engel, C. J.; Hryn, A. J.; Odom, T. W. Polymer Nanowrinkles with Continuously Tunable Wavelengths. *ACS Appl. Mater. Interfaces* **2013**, *5*, 6438–6442.
- (102) Bayley, F. A.; Liao, J. L.; Stavrinou, P. N.; Chiche, A.; Cabral, J. T. Wavefront kinetics of plasma oxidation of polydimethylsiloxane: Limits for sub-mm wrinkling. *Soft Matter* **2014**, *10*, 1155–1166.
- (103) Wang, Q.; Zhao, X. A three-dimensional phase diagram of growth-induced surface instabilities. *Sci. Rep.* **2015**, *5*, 8887.
- (104) Leibler, L.; Sekimoto, K. On the sorption of gases and liquids in glassy polymers. *Macromolecules* **1993**, *26*, 6937–6939.
- (105) Bar, A.; Ramon, O.; Cohen, Y.; Mizrahi, S. Shrinkage behaviour of hydrophobic hydrogel during dehydration. *J. Food Eng.* **2002**, *55*, 193–199.
- (106) Sekimoto, K. Temperature hysteresis and morphology of volume phase transition of gels. *Phys. Rev. Lett.* **1993**, *70*, 4154–4157.
- (107) de Gennes, P.-G. Solvent evaporation of spin cast films: “crust” effects. *Eur. Phys. J. E* **2002**, *7*, 31–34.
- (108) Talini, L.; Lequeux, F. Formation of glassy skins in drying polymer solutions: Approximate analytical solutions. *Soft Matter* **2023**, *19*, 5835–5845.
- (109) Kodio, O.; Griffiths, I. M.; Vella, D. Lubricated wrinkles: Imposed constraints affect the dynamics of wrinkle coarsening. *Phys. Rev. Fluids* **2017**, *2*, 014202.
- (110) Stafford, C. M.; Harrison, C.; Beers, K. L.; Karim, A.; Amis, E. J.; Vanlandingham, M.; Kim, H.-C.; Volksen, W.; Miller, R. D.; Simonyi, E. E. A buckling-based metrology for measuring the elastic moduli of polymeric thin films. *Nat. Mater.* **2004**, *3*, 545–550.
- (111) Weiss, F.; Cai, S.; Hu, Y.; Kyoo Kang, M.; Huang, R.; Suo, Z. Creases and wrinkles on the surface of a swollen gel. *J. Appl. Phys.* **2013**, *114*, 073507.
- (112) Cerdá, E.; Mahadevan, L. Geometry and physics of wrinkling. *Phys. Rev. Lett.* **2003**, *90*, 074302.
- (113) Bowden, N.; Brittain, S.; Evans, A. G.; Hutchinson, J. W.; Whitesides, G. M. Spontaneous formation of ordered structures in thin films of metals supported on an elastomeric polymer. *Nature* **1998**, *393*, 146–149.
- (114) Davis, C. S.; Crosby, A. J. Mechanics of wrinkled surface adhesion. *Soft Matter* **2011**, *7*, 5373–5381.
- (115) Niven, J. F.; Chowdhry, G.; Sharp, J. S.; Dalnoki-Veress, K. The emergence of local wrinkling or global buckling in thin freestanding bilayer films. *Eur. Phys. J. E* **2020**, *43*, 20.
- (116) Genzer, J.; Groenewold, J. Soft matter with hard skin: From skin wrinkles to templating and material characterization. *Soft Matter* **2006**, *2*, 310–323.
- (117) Gurmessa, B. J.; Croll, A. B. Localization in an idealized heterogeneous elastic sheet. *Soft Matter* **2017**, *13*, 1764–1772.
- (118) Karpitschka, S.; Eggers, J.; Pandey, A.; Snoeijer, J. H. Cusp-Shaped Elastic Creases and Furrows. *Phys. Rev. Lett.* **2017**, *119*, 198001.
- (119) Moore, M. R.; Vella, D.; Oliver, J. M. The nascent coffee ring: How solute diffusion counters advection. *J. Fluid Mech.* **2021**, *920*, A54.